

IMPACTS OF SOURCE PROPERTIES ON STRONG LENSING BY RICH GALAXY CLUSTERS

G. J. GAO^{1,2}, Y. P. JING¹, S. MAO³, G. L. LI^{1,4}, X. KONG⁵

¹ Key Laboratory for Research in Galaxies and Cosmology, Shanghai Astronomical Observatory, Chinese Academy of Sciences, 80 Nandan Road, Shanghai, 200030, China

² Graduate School of the Chinese Academy of Sciences, Beijing, 100039, China

³ Jodrell Bank Centre for Astrophysics, School of Physics and Astronomy, University of Manchester, Manchester M13 9PL, UK

⁴ Argelander-Institut für Astronomie, Auf dem Hügel 71, Bonn D-53121, Germany and

⁵ Key Laboratory for Research in Galaxies and Cosmology, University of Science and Technology of China, Chinese Academy of Sciences, Hefei, 230026 China

Draft version November 12, 2018

ABSTRACT

We use a high-resolution N -body simulation to investigate the influence of background galaxy properties, including redshift, size, shape and clustering, on the efficiency of forming giant arcs by gravitational lensing of rich galaxy clusters. Two large sets of ray-tracing simulations are carried out for 10 massive clusters at two redshifts, i.e. $z_1 \sim 0.2$ and 0.3 . The virial mass (M_{vir}) of the simulated lens clusters at $z \sim 0.2$ ranges from $6.8 \times 10^{14} h^{-1} M_{\odot}$ to $1.1 \times 10^{15} h^{-1} M_{\odot}$. The information of background galaxies brighter than 25 magnitude in the I -band is taken from Cosmological Evolution Survey (COSMOS) imaging data. Around 1.7×10^5 strong lensing realizations with these images as background galaxies have been performed for each set. We find that the efficiency for forming giant arcs for $z_1 = 0.2$ clusters is broadly consistent with observations. Our study on control source samples shows that the number of giant arcs is decreased by a factor of 1.05 and 1.61 when the COSMOS redshift distribution of galaxies is adopted, compared to the cases where all the galaxies were assumed to be in a single source plane at $z_1 = 1.0$ and $z_1 = 1.5$, respectively. We find that the efficiency of producing giant arcs by rich clusters is weakly dependent on the source size and clustering. Our principal finding is that a small proportion ($\sim 1/3$) of galaxies with elongated shapes (e.g. ellipticity $\epsilon = 1 - b/a > 0.5$) can boost the number of giant arcs substantially. Compared with recent studies where a uniform ellipticity distribution from 0 to 0.5 is used for the sources, the adoption of directly observed shape distribution increases the number of giant arcs by a factor of ~ 2 . Our results indicate that it is necessary to account for source information and survey parameters (such as point-spread-function, seeing) to make correct predictions of giant arcs and further to constrain the cosmological parameters.

Subject headings: gravitational lensing – galaxies: clusters: general – dark matter – methods: data analysis

1. INTRODUCTION

Giant arcs are spectacular examples of strong gravitational lensing found in rich galaxy clusters. Background galaxies are stretched into long, thin arcs by the intense foreground gravitational field. Hundreds of giant arcs have been found in both optically-selected and X-ray selected clusters (e.g. Luppino et al. 1999; Zaritsky & Gonzalez 2003; Gladders et al. 2003; Sand et al. 2005).

Massive clusters are efficient producer of giant arcs and the number of giant arcs is a good indicator of the abundance of massive clusters. The halo mass function is very sensitive to the cosmological parameters, especially at the massive end. Moreover, the internal structures of massive clusters, such as substructures and ellipticity, also depend on the cosmological parameters. They all affect the lensing probability (optical depth, e.g., Meneghetti et al. 2003a,b; Wambsganss et al. 2004; Torri et al. 2004; Dalal et al. 2004; Li et al. 2005; Oguri et al. 2003, 2008; Hilbert et al. 2007; Puchwein et al. 2005, 2009) in various degree. Therefore, the observation of giant arcs is a useful probe of the cosmological model, in particular the matter power-spectrum normalization, σ_8 (Li et al. 2006b), the matter density, $\Omega_{m,0}$, and to a less extent the cosmological constant, $\Omega_{\Lambda,0}$.

However, in order to use the observations of giant arcs to constrain the cosmological models, one has to thoroughly understand how the lensing probability is affected by the distribution of background source galaxies, as well as the intrinsic properties of lens population. It has been shown that the lensing probability increases significantly with the increase of the source redshift, thus it is necessary to quantify the redshift distribution of source galaxies in lensing studies (Wambsganss et al. 2004). The lensing efficiency of massive clusters does not depend on the source size significantly (Li et al. 2005), although not all the real source information has been used, in particular their shapes.

Horesh et al. (2005) first adopted realistic galaxy images with known photometric redshifts from the Hubble Deep Field (HDF) as background sources. They selected clusters from a cosmological N -body simulation in a $\sim 140 h^{-1} \text{Mpc}$ box at $z_1 \sim 0.2$. The mass of the simulated lens clusters ($0.54\text{--}1.1 \times 10^{15} h^{-1} M_{\odot}$) is similar to that of 10 X-ray-selected

clusters (Smith et al. 2005), the (mean) mass range of which is around $6.3 \times 10^{14} h^{-1} M_{\odot} \leq M_{200} \leq 2.0 \times 10^{15} h^{-1} M_{\odot}$. Note that the mass is calculated based on the X-ray luminosity by using the L_x - M_{200} relation (Reiprich & Böhringer 2002). They argued that the probability of producing giant arcs is ~ 1 per cluster after observational effects are included, and emphasize that the number of giant arcs produced by the simulated clusters in their adopted cosmology (with $\Omega_{m,0} = 0.3, \Omega_{\Lambda,0} = 0.7$ and the power-spectrum normalization of $\sigma_8 = 0.9$) is consistent with the one observed in the massive clusters at redshift $0.171 < z_c < 0.255$.

In this paper, we focus on the impact of background galaxy properties, rather than the properties of the lens clusters, on the efficiency of producing giant arcs. We use the COSMOS data as direct input for the properties of background galaxies. We investigate how the strong lensing probabilities are affected by the shape, size, redshift distributions and clustering of background galaxies. Instead of adopting all these source properties as a whole (Horesh et al. 2005), we vary each of the source properties in turn to gain a clear understanding about their individual impacts on strong lensing statistics. The COSMOS data has a substantial advantage over the HDF as it covers a much larger sky area (its sky coverage is 1.6 square degrees vs. 5.3 square arcmins for the HDF) as used in Horesh et al. (2005), and thus is less affected by the cosmic variance. While we confirm the effects of source redshift and size distributions, we find that the shape distribution of real galaxies has a dramatic effect on the lensing probability. With the COSMOS images, the lensing probability is boosted by a factor of 2 relative to that based on simple assumptions of the shape distribution (e.g. random ellipticity between 0 and 0.5). Our results indicate that the shape of galaxies is an important factor in matching the theoretical predictions and the observations of giant arcs. We will also show that clustering of background galaxies has a negligible effect on the lensing efficiency of producing giant arcs.

This paper is structured as follows. In §2, we discuss COSMOS and background source population. In §3, we discuss the simulation we use and our lensing methodology. In §4, we present our main results and compare with recent studies. We finish in §5 with a short summary and a brief discussion of the implications of our results.

2. COSMOS AND BACKGROUND SOURCE POPULATION

COSMOS is a deep survey covering a 2 square degrees of equatorial field containing over 2 million galaxies. It is an ideal sample of background galaxies for our lensing simulations due to the excellent resolution and large survey area (to reduce the cosmic variance). The image is centered on RA=10:00:28.6 and DEC=+02:12:21.0 from the Hubble Space Telescope Advanced Camera for Surveys (HST/ACS) (Koekemoer et al. 2007). Its calibration is relatively reliable due to the absence of atmospheric absorption. The *I*-band image data we use is the second public release of COSMOS observations. The camera has two 2048×4096 CCD chips with a pixel scale of $0.05''$. All the drizzled image data have been flux calibrated and astrometrically registered. The whole image in the *I*-band has been cut into 575 edge-overlapped tiles of 4960×4960 pixels of CCD, which are generated by rotating with an angle of ~ 10 degrees to the tile edge and embedded at the center of a rectangular box of 5600×5600 pixels. The left area in the box is empty of galaxies.

The galaxy images in the COSMOS field are identified with the SExtractor program (Bertin & Arnouts 1996). The SExtractor is a well developed software program for extracting galaxy images from raw data and it produces a catalog of objects including properties such as their morphology, positions and magnitudes. The SExtractor detection threshold for all the ACS image data is set to be 1.5σ which is about 25mag/arcsec² in surface brightness. Finally, a total of $\sim 3 \times 10^5$ galaxies are identified. The output of SExtractor contains the relative positions of sources in the tile and positions in the celestial equator coordinate system. The relative position is useful for identifying which galaxies are strongly lensed in the lensing process (see §3.2). The celestial coordinates of galaxies are matched with the positions in COSMOS photometric catalog (Mobasher et al. 2007) of galaxies brighter than *I*-band AB magnitude of 25 to obtain the redshift information. Only the galaxies successfully matched, thus having correct photometric redshifts, are added in our lensing simulations. Using the COSMOS mask catalog, we exclude all star-like sources, galaxies close to star-like sources, and those possibly contaminated by spikes due to the overflow of CCD pixels. In particular, we use the same shape analysis program as in search for giant-arcs (see §3.2) to identify very elongated sources with the major-axis to minor-axis ratio ≥ 10 in all the tiles and exclude them to avoid ‘‘giant-arc like’’ artifact sources (e.g. imperfectly masked spikes due to CCD pixel overflow and asteroid trails) or real sources which could have been lensed by foreground objects in COSMOS field.

All the cleaned COSMOS tiles are added behind the lens clusters as source patches. The sky coverage of strong lensing simulation is the same as the original COSMOS field. Due to the magnitude limit of the photometric catalog, the density of matched galaxies with photometric redshift is about 500 per tile of 5600×5600 pixels ($\sim 4.13 \times 4.13$ square arcmins) which contains 4096×4096 effective CCD pixels. Thus, the surface number density of the extracted galaxies is about 43 galaxies arcmin⁻² in the CCD imaging area. Tiles of 5600×5600 pixels with white margin are placed randomly behind the lensing clusters in the lensing simulation, without specifically requiring that the lensing caustic area falls within the actual image. This reduces the effective source number density to ~ 23 galaxies arcmin⁻² in our lensing analysis.

The scatter plots of source size (in pixels) vs. redshift, the ellipticity (ϵ) vs. redshift and ellipticity vs. source size with the median (as red filled circle) and the 68% value range (as red bars) for 20 randomly selected source tiles are shown in Figs. 1-3. The ellipticity ϵ is quantified by $1 - b/a$, where b and a are semi-minor and semi-major axes of a galaxy image. The axes are obtained by fitting the image with an ellipse using the same method as that for quantifying the shape of giant arcs (see §3.2). Fig. 1 shows that the sources become smaller as the redshift increases from 0 to ~ 2 , and then remain flat out to redshift $z = 3.0$. However, the ellipticity of galaxies is almost independent of redshift (see Fig. 2). The source size and ellipticity are somewhat correlated (especially for the sources of the effective diameter

smaller than $\sim 1.2''$, as can be seen in Fig. 3 – larger sources appear to be somewhat more elliptical.

The photometric redshift distribution of COSMOS background galaxies is plotted (as the black solid line) in Fig. 4 for all the galaxies in 575 tiles of COSMOS field. As can be seen the redshift distribution peaks around $z = 0.8$, but extends out to $z = 3.0$ with a median redshift of 0.78. The histogram is well fitted by the empirical formula from Smail et al. (1995):

$$p(z_s) = \frac{\beta}{z_0^3 \Gamma(3/\beta)} z_s^2 \exp\left[-\left(\frac{z_s}{z_0}\right)^\beta\right], \quad (1)$$

where $z_0 \sim 0.5$ and $\beta \sim 1.2$; the best-fit line is indicated as the black dashed line in Fig. 4.

With the photometric redshifts, we can construct an approximately three-dimensional distribution of background galaxies in order to study the effect of source redshift distribution on strong lensing efficiency. A series of source planes perpendicular to the line of sight is set between redshift $z_1 \sim 0.2$ (~ 0.3) to $z_s = 3.0$. The redshift separation between two adjacent source planes δz is set to $\delta z/z = 0.1$ for $1.5 < z \leq 3.0$ and to $\delta z/z = 0.05$ for $0.2 < z \leq 1.5$. The galaxies are projected onto the planes according to which redshift bin they fall in. In each source plane, we mark all the galaxy pixels, which are used to identify the lensed sources in subsequent ray-tracing. There are 48 source planes in total for the ray-tracing program (see §3.2).

We will also study the impact of ellipticity and size distributions on lensing cross-sections. The ellipticity distribution of the COSMOS galaxies are illustrated (as the black solid histogram) in Fig. 5. The ellipticity $1 - b/a$ distribution has a median of 0.4, which is similar to that presented in Ferguson et al. (2004). Compared to the studies of giant arcs using a uniform distribution of the ellipticity with $0 \leq 1 - b/a \leq 0.5$ for background sources, COSMOS clearly has an extended tail of highly flattened galaxies, which will have a significant impact on the efficiency of forming giant arcs (see §4.1.2).

The size of each galaxy is quantified by an effective diameter D_{eff} defined as the diameter of a circular-shaped galaxy with the same number of the image pixels. The size distribution of galaxies in these tiles is shown (as the black solid line) in Fig. 6. The size distribution of galaxies has a peak at $D_{\text{eff}} \sim 0.75''$, but ranges from effective diameter $D_{\text{eff}} < 0.2''$ to $D_{\text{eff}} > 2''$. The median diameter of background galaxies is about $0.6''$, smaller than that assumed to be $D_{\text{eff}} = 1''$ (Li et al. 2005) since a relatively deeper galaxy survey is adopted in this work.

3. NUMERICAL SIMULATION AND LENSING METHODOLOGY

3.1. Simulated Clusters

The lens clusters are selected from a N -body simulation generated with an upgraded version of vectorized-parallel P³M code of Jing & Suto (2002) (Jing, Suto & Mo 2007). The underlying cosmological model is a Λ CDM ($\Omega_{m,0} = 0.268$, $\Omega_{\Lambda,0} = 0.732$, $n = 1$) model. The simulation uses 1024^3 dark matter particles in a box with a side length of $600h^{-1}$ Mpc (comoving). The mass resolution is $1.5 \times 10^{10} h^{-1} M_\odot$, thus massive clusters are reasonably resolved (with more than 4×10^4 particles in our samples). In this simulation (refer to Jing, Suto & Mo (2007) for more details), the Hubble constant h in unit of $100 \text{ km s}^{-1} \text{ Mpc}^{-1}$ is taken to be 0.71, while the amplitude of the linear density power spectrum, σ_8 , is 0.85, which is obtained from CMBFAST (Seljak & Zaldarriaga 1996) directly. Particle pairwise interactions are softened on scales smaller than $30 h^{-1} \text{ kpc}$. The clusters are identified by the Friends-Of-Friends (FOF) method with a linking length of 0.2 times the mean particle separation, and the cluster mass M_{vir} is defined as the mass enclosed within the virial radius according to the spherical collapse model (Kitayama & Suto 1996; Bryan & Norman 1998; Jing & Suto 2002).

We primarily use a sample of 10 massive clusters at redshift $z \sim 0.2$ to perform ray-tracing simulations. This is to facilitate comparisons with observations of the X-ray selected cluster sample (Smith et al. 2005). The mass of the massive clusters at redshift $z \sim 0.2$ ranges from $6.8 \times 10^{14} h^{-1} M_\odot$ to $1.1 \times 10^{15} h^{-1} M_\odot$, roughly consistent with the observed range of mass ($6.3 \times 10^{14} \leq M_{200} \leq 2.0 \times 10^{15} h^{-1} M_\odot$ of clusters at redshift $0.171 < z_c < 0.255$).¹ We shall also use 10 most massive clusters at $z \sim 0.3$ for lensing efficiency comparisons.

3.2. Ray-tracing and Mapping

We use the thin lens plane approximation for the lensing calculation; the line of sight contributions may be important (Wambsganss et al. 2004; Puchwein et al. 2009). The surface density is calculated on a mesh of 1024×1024 (coarse) grids centered at the cluster with a size of 2 times the virial radii. Our smoothing method, similar to Li et al. (2006a), uses the smoothed particle hydrodynamics kernel (Monaghan et al. 1992) to distribute the mass of particles enclosed inside the virial radius of the lens onto 3-D grids and then the surface density is obtained by integrating along the line of sight. The dimensionless surface density (κ) map is obtained by dividing the surface density by the critical value,

$$\Sigma_{\text{cr}} = \frac{c^2}{4\pi G} \frac{D_s}{D_1 D_{1s}}, \quad (2)$$

where D_s , D_1 , and D_{1s} are the angular diameter distances between the source and the observer, the lens and the observer, and the source and the lens. The lensing potential on the grids of the coarse mesh, ϕ , is calculated by the

¹ Notice that M_{200} is defined as the mass enclosed within r_{200} , the radius within which the average density is equal to 200 times the critical cosmological density. The difference between M_{200} and M_{vir} are within 10% for 8 of 10 clusters. It is within 30% for the other two clusters.

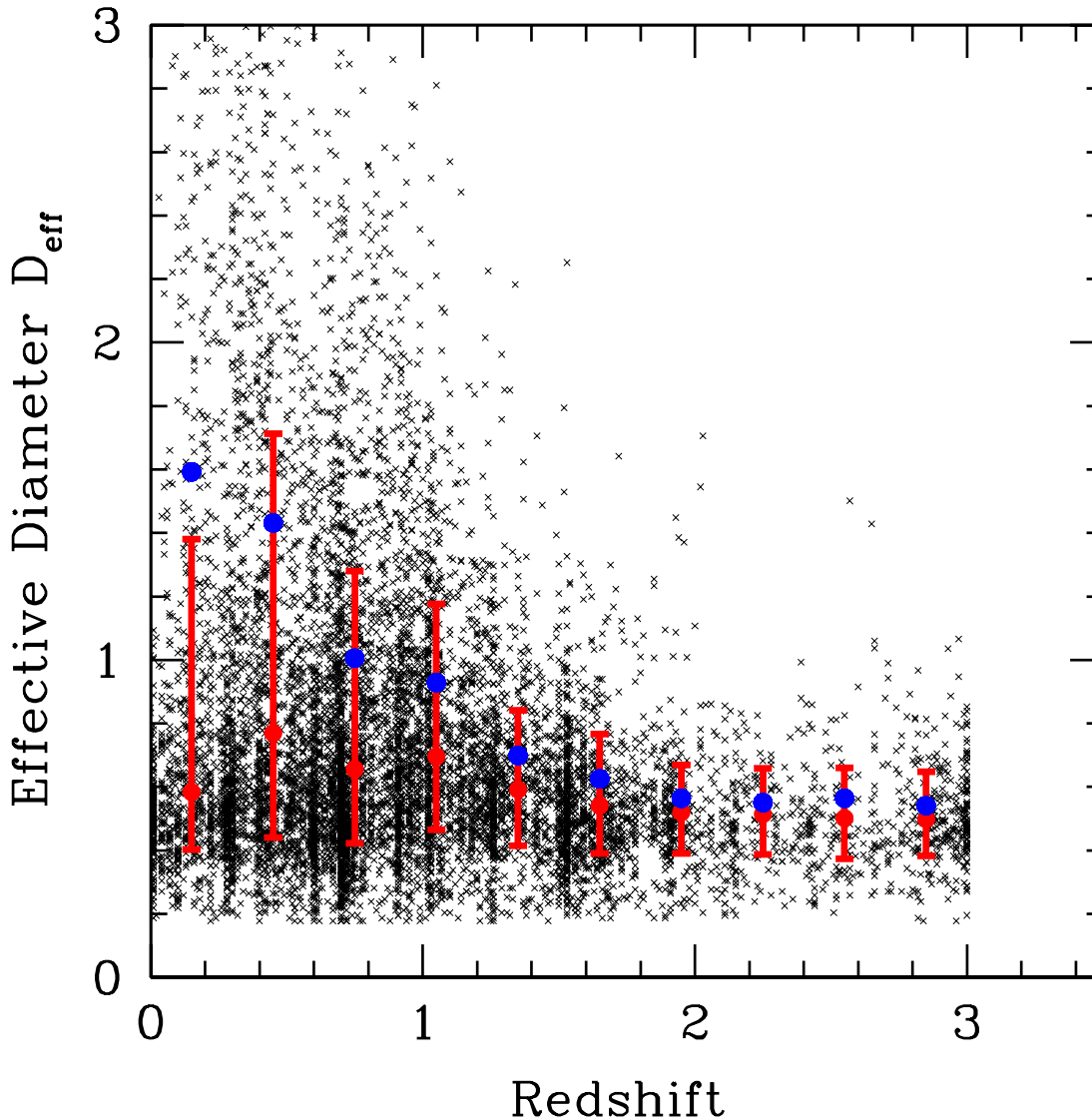


FIG. 1.— The scatter plot of size against redshift for galaxies randomly selected from 20 COSMOS image tiles with a bin width of $\Delta z = 0.3$. Each tile has 4096×4096 effective pixels (with a pixel scale of 0.05 arcsec by 0.05 arcsec) covering a field of view of 3.4 arcmins by 3.4 arcmins. The median (red filled circle) and the 68% source size range (red bar) are indicated in 10 bins of redshift. As can be seen, the source size distribution is almost independent of the redshift. For comparison with Ferguson et al. (2004), the mean value (blue filled circle) of effective diameter in each redshift bin is also plotted. As our survey depth is much shallower, they actually agree well with each other.

Fast Fourier Transform (FFT) method from the dimensionless surface density map since they are related by $\nabla^2 \phi = 2\kappa$. The shear (γ) is then obtained by the second-order derivatives of the potential, and the (signed) magnification is given by $\mu^{-1} = (1 - \kappa)^2 - \gamma^2$.

To better determine the geometry of an image and to perform an efficient lensing simulation, we refine the cell size of the central high magnification area with $|\mu| \geq 2.5$ in the lens plane up to $0.05''$, identical to the intrinsic observational resolution in the source planes. High resolution is necessary for resolving the lensed image well, especially in the direction of minor axis, which is much more sensitive to the resolution. The lensing potential on the refined mesh is obtained by cubic spline interpolations of the neighboring 14×14 coarse grids in the 1024×1024 mesh. Once we obtain the lensing potential in the whole fine mesh area of interests, the deflection angle on each grid point can be calculated from the derivative of the lensing potential, $\vec{\alpha} = \nabla \phi$. The lens mapping from the lens plane to each source plane at different redshifts can be constructed using the lens equation (i.e. ray-tracing), $\vec{y} = \vec{x} - \vec{\alpha}$, where \vec{y} , \vec{x} are dimensionless source position in source plane and image position in lens plane. The ray-tracing procedure is repeated for each of the ~ 50 source planes, as we discussed in §2.

We identify the image pixels in the lens plane from the mapping between the lens plane and the source planes. For each projection of a lens, we go through all the refined grid points one by one and check whether there is a

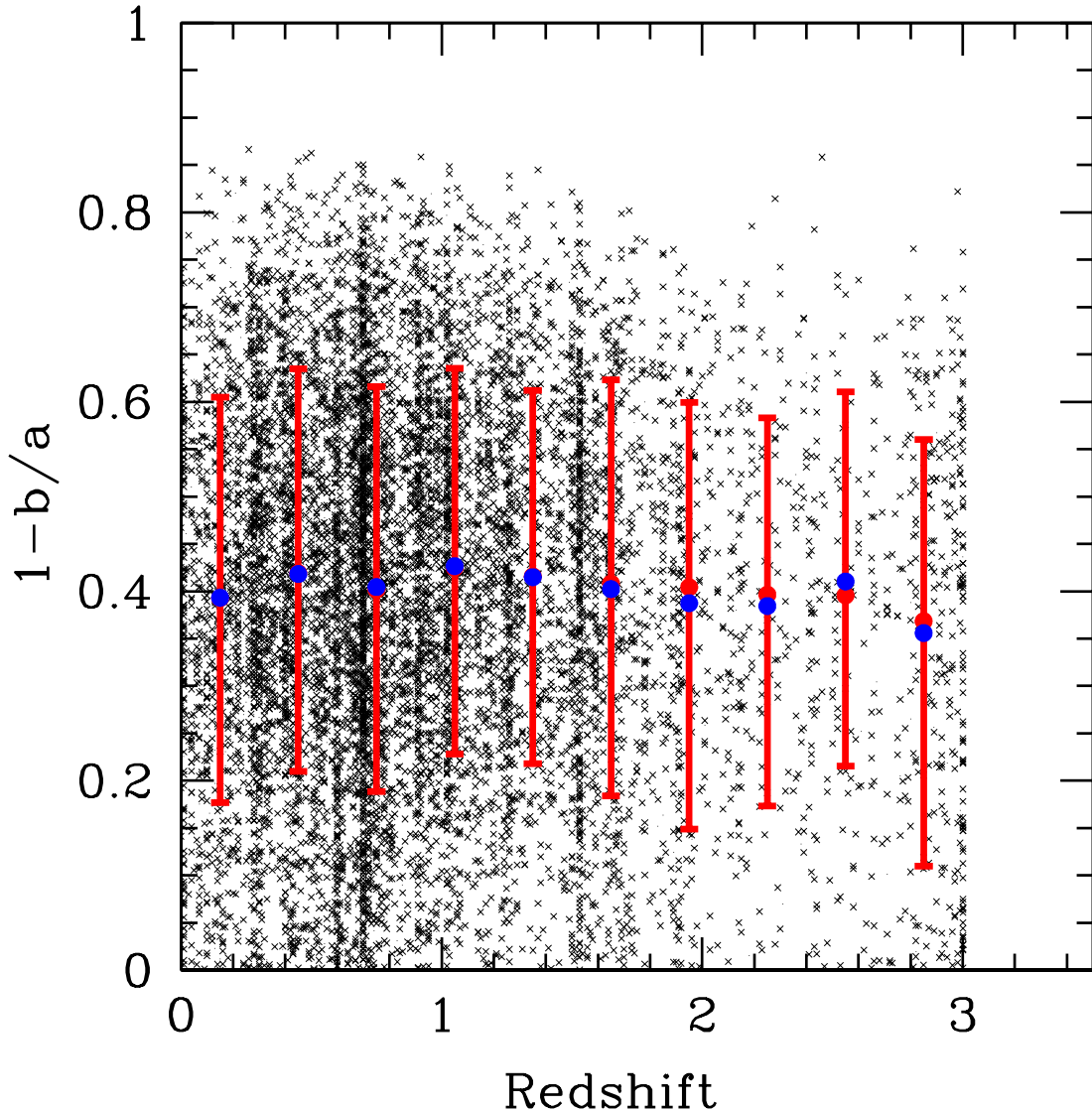


FIG. 2.—: The scatter plot of the ellipticity, $\epsilon = 1 - b/a$, against redshift for galaxies randomly selected from 20 tiles with a bin width of $\Delta z = 0.3$. The median (red filled circle) and the 68% ellipticity range (red bar) are indicated in 10 bins of redshift. As can be seen, the source ellipticity distribution is randomly distributed at all the redshifts. The mean value (blue filled circle) of ellipticity in each redshift bin is also plotted for comparison.

corresponding point in the source planes falling into a galaxy. If so, we identify this grid point in the image plane as a lensed image pixel of that source galaxy; if not, it is a trivial grid. All the highly magnified lensed image pixels (e.g., $|\mu| \geq 2.5$) can be located. Finally, we can obtain the whole image(s) of a background galaxy by collecting all the image pixels of the same source using Friends-of-Friends (FOF) method.

For source slices at different redshifts, the high-magnification areas will be mapped into areas of different sizes in the sky. We choose a rectangular conjunctive angular area inclusive of every caustic area and put this angular box randomly in the source tile to select different background galaxies for the ray-tracing simulation. The box size is usually on the level of a few square arcmins (depending on projection and also mass profile). Since each added source tile is about $4.7' \times 4.7'$, around 10 random lensing realizations are needed to cover a tile effectively. To avoid boundary effects, the source tile is periodically expanded in both dimensions which are then randomly sampled.

The same process is carried out for all the three orthogonal projections of the massive clusters at the expected redshifts. 10 ray-tracing simulations are carried out with all source galaxy samples in the COSMOS field for each of 3 orthogonal projections. The lensing images found are stored and subject to more detailed analysis to find their length-to-width (L/W) ratios, sizes, the redshifts. Of particular importance is the L/W ratio. We determine this quantity following Bartelmann et al. (1998) and Li et al. (2005). Briefly, we first identify the center of the image pixels for a given source (\vec{x}_c), and then locate the point \vec{x}_1 that is the furthest from the centre, and finally the point \vec{x}_2 that is the furthest from \vec{x}_1 . We then fit a circular arc that passes through these three points ($\vec{x}_1, \vec{x}_2, \vec{x}_c$). The half length

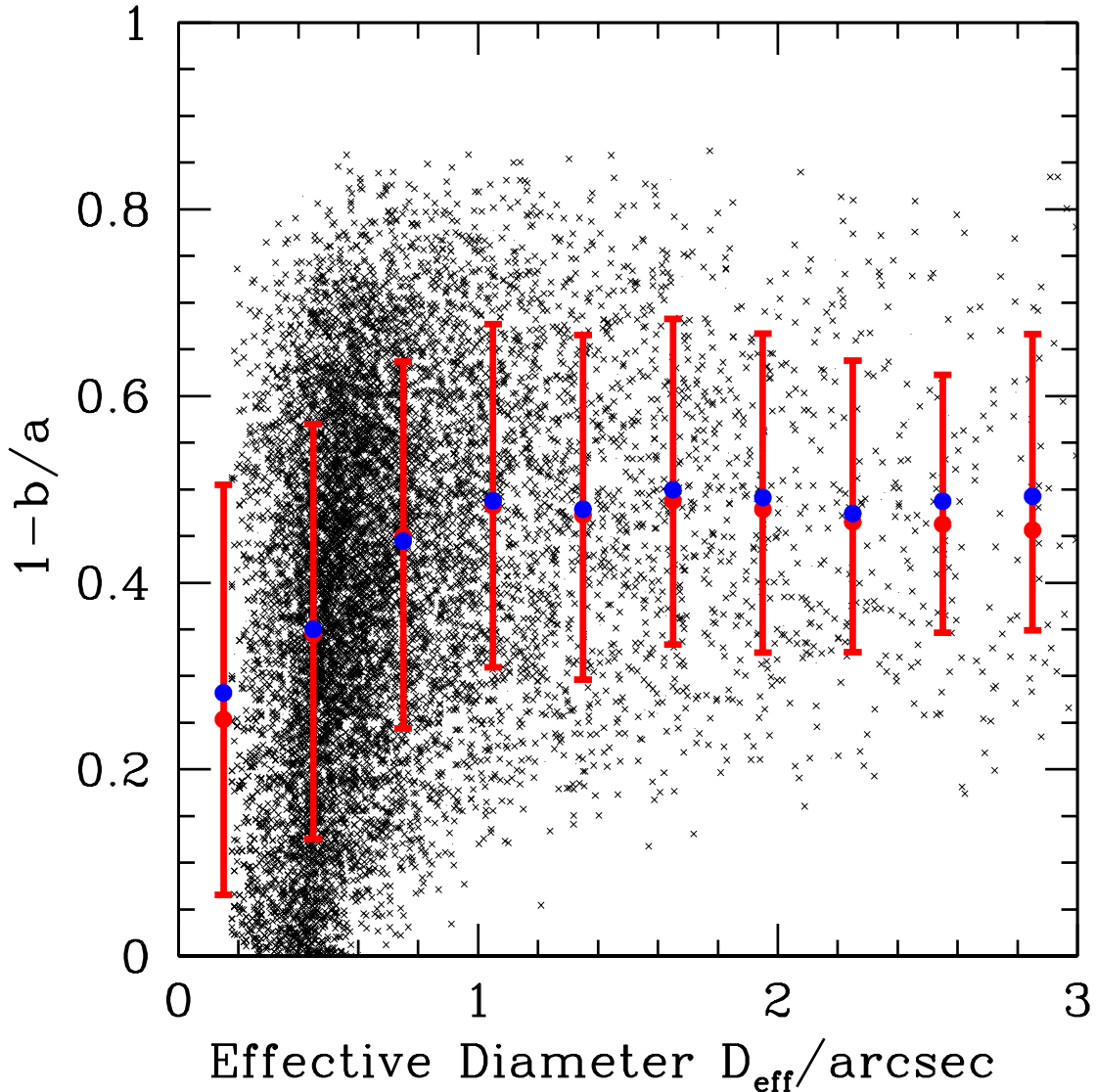


FIG. 3.— The scatter plot of the ellipticity, $\epsilon = 1 - b/a$, against size of galaxies in 20 randomly selected tiles with a bin width of $\Delta D_{\text{eff}} = 0.3$. The median (red filled circle) and the 68% ellipticity range (red bars) are indicated in 10 bins of effective diameter D_{eff} . The galaxies are more elliptical as the size increases for sources with the effective diameter smaller than $\sim 1.2''$, while the median ellipticity keeps around 0.5 for the left size range. The mean value (blue filled circle) of ellipticity in each effective diameter bin is also plotted for comparison.

of the arc is taken to be the semi-major axis length of the ellipse, a , and the length of the semi-minor axis is taken to be $b = S_{\text{image}}/(\pi a)$, where S_{image} is the area covered by the image. The length-to-width ratio is then simply a/b . As mentioned before, the same procedure is used to determine the ellipticity, $1 - b/a$, for unlensed galaxies.

3.3. Simulating test images

We carried out a test by putting a source around the tangential caustic curve (as the green dotted line) of a massive simulated cluster. The simulated images (shown in red) are illustrated in Fig. 7 together with the source (shown in black) positions. As expected, it produces one, two and three images when the mocked source is outside, on and inside the caustic curve. Fig. 8 shows a simulated image of a massive lens cluster of a realization based on a real source tile. Clearly, the sources (shown in black) have been systematically stretched around the cluster center. In particular, there is one giant arc at redshift $z = 2.52$ (labeled as “A1”) with $L/W \sim 22$ among the lensed images produced from source “a”, which has an additional image labeled as “A2”. Notice that the positions of the images and background galaxies in different planes are transformed into the same coordinate system centered at the cluster centre.

4. RESULTS

Many recent studies have shown that the efficiency of forming giant arcs depends on the background source population, in particular, their sizes and redshifts (e.g., Wambsganss et al. 2004; Li et al. 2005; Horesh et al. 2005). Since

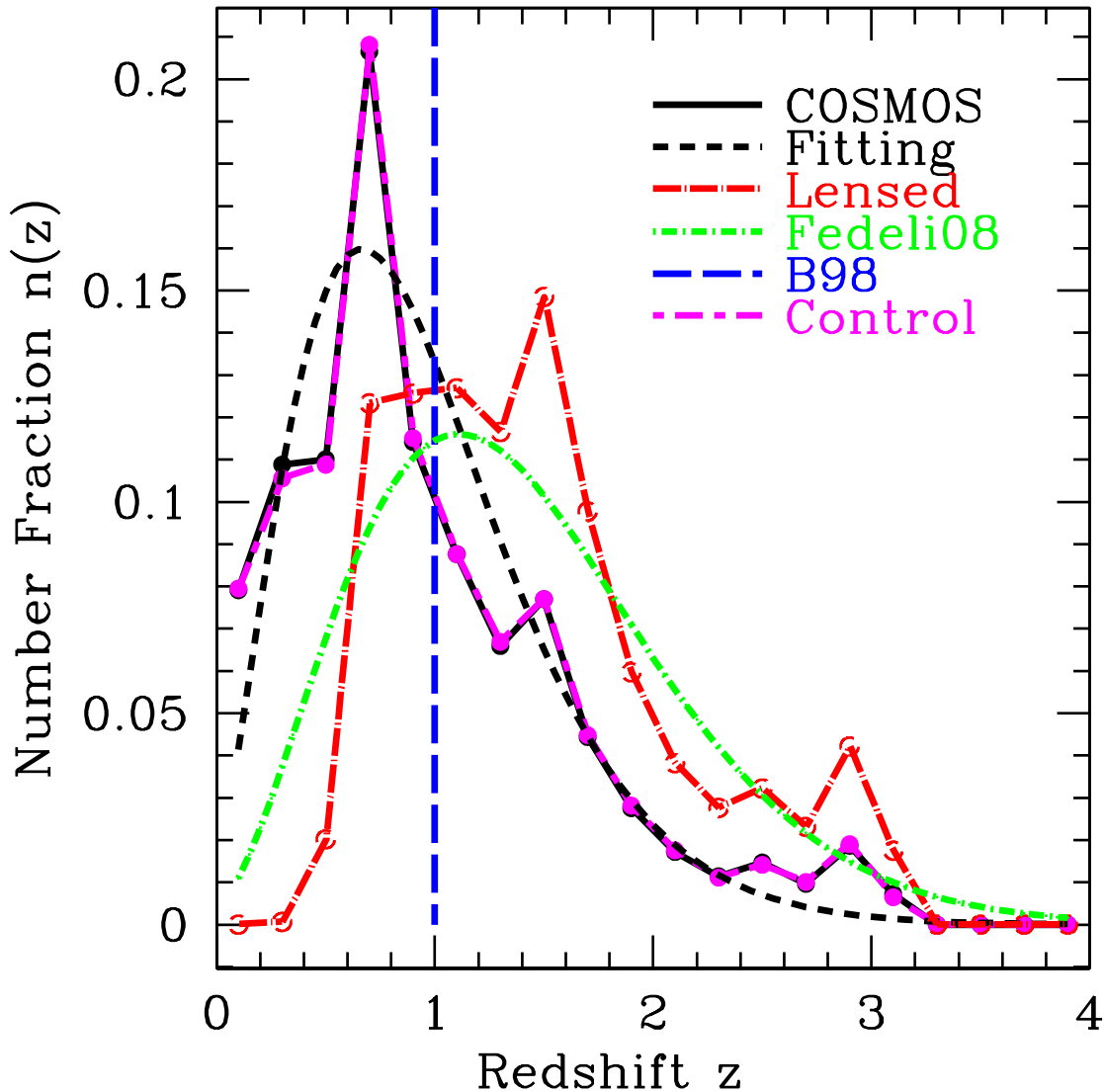


FIG. 4.— Comparison plot of redshift probability distributions between the subpopulation of original galaxies which have been strongly lensed to be arcs of $L/W \geq 10$ ($z_1 = 0.2$) and the parent population of COSMOS galaxies. The number fractions per redshift bin of width $\Delta z = 0.2$ are plotted. The lensed population is clearly shifted toward high-redshift end. The fitting curve of the COSMOS redshift by Eq. 1 is indicated as the black dashed line. The redshift distribution of the fiducial control sample consisting of 100 randomly selected tiles (used in Table 1), which roughly follows the mean distribution, is plotted in magenta. For comparison, the redshift distributions used in Bartelmann et al. (1998) and Fedeli et al. (2008) are also shown.

different giant arc surveys have different selection effects, the goal of this work is not only to compare our strong lensing efficiency with observations, but also to focus on using realistic, empirical information of background sources, and then to study how the lensing efficiency changes as we vary the assumptions.

For this purpose, we construct 7 comparison source samples in the control group which will be added in the ray-tracing simulations. All the samples are based on 100 randomly selected COSMOS tiles. The mean number density of this control sample is around 500 galaxies per tile, which is the same as the mean density from the whole field. The sample with COSMOS background sources is our fiducial case (Case 1). This sample also provides the basis on which we generate mocked samples with partially or fully artificial source properties for Cases from 2 to 7. The artificial sources are mocked tile by tile. The lensing simulations are performed for 3 projections of 5 massive clusters. For effectively sampling the source area, 10 realizations are carried out for each projection in each source tile. There are 15000 simulations in total for each case. The resulting arc statistics for this control group (e.g. six mocked samples together with the COSMOS sample) are listed in Table 1. The lensing efficiency changes as different source properties are switched. We find source properties affects the lensing efficiency in various degrees by comparing the numbers of giant arcs between different cases, especially the source ellipticity and redshift. Furthermore, we also find that the

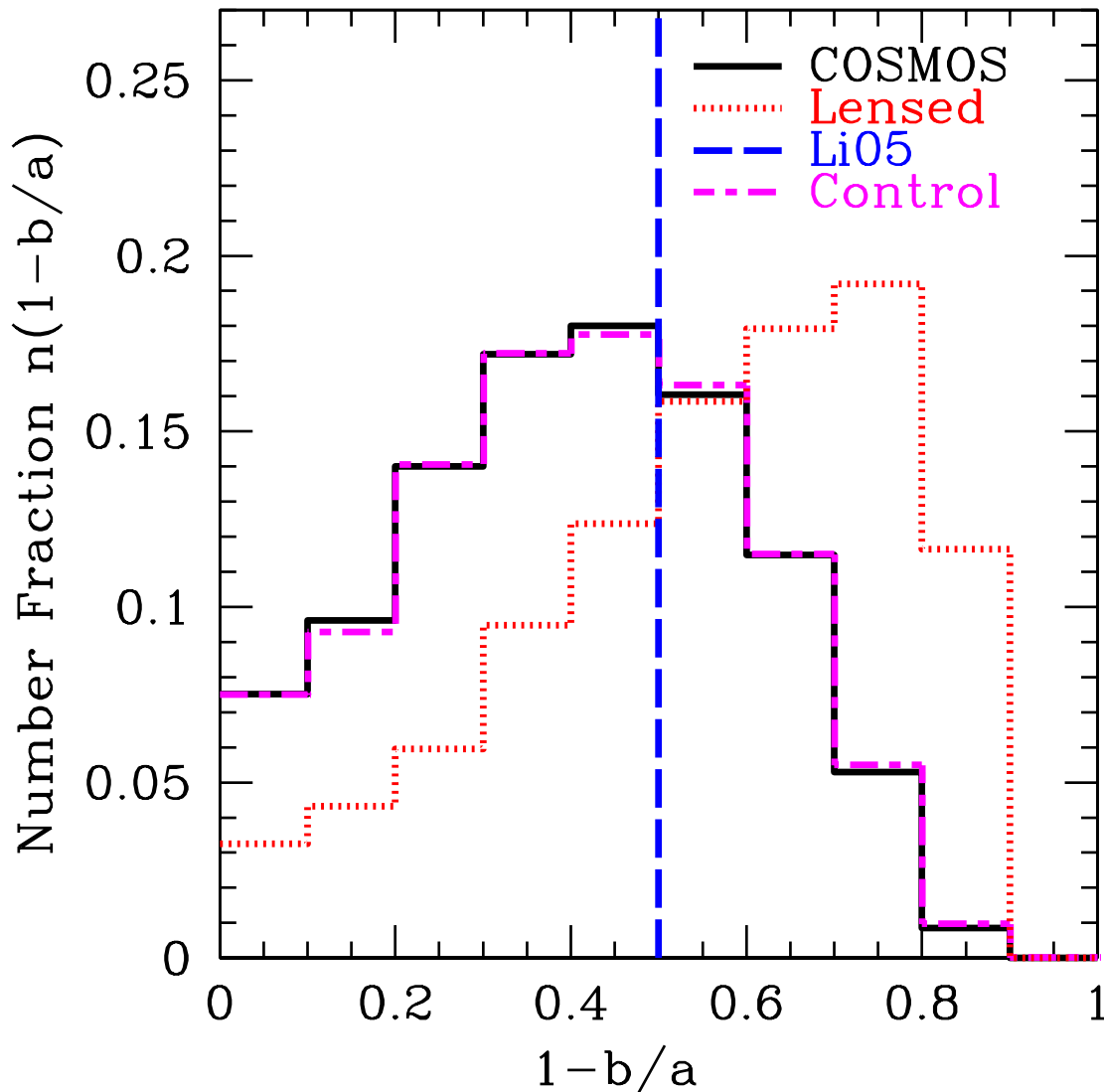


FIG. 5.— Comparison plot of shape probability distributions between the subpopulation of original galaxies which have been strongly lensed to be arcs of $L/W \geq 10$ ($z_1 = 0.2$) and the parent population of COSMOS galaxies. The number fractions per ellipticity bin of width $\Delta\epsilon = 0.1$ are plotted. The lensed population clearly shows a bias towards high ellipticity compared with the original distribution. The shape distribution of the fiducial control sample consisting of 100 randomly selected tiles (used in Table 1) is plotted in magenta and agrees with COSMOS distribution very well. For comparison, the distribution used in Li et al. (2005) is also shown.

boosting factor due to the source ellipticity on lensing efficiency depends on the source redshift. The details are listed below.

4.1. Lensing efficiency of COSMOS sources

Using the empirical COSMOS background source information, and the method outlined in the last section, we implement a mock lensing survey for each projection of the massive clusters at redshift $z_1 = 0.2$ and $z_1 = 0.3$ for all of 575 tiles from COSMOS (Table 2). We adopt the definition of the L/W ratio of Li et al. (2005). In total, 12816 giant arcs of $L/W \geq 10$ are found out of 172500 cases at $z_1 = 0.2$, while 9704 giant arcs for clusters at $z_1 = 0.3$. Therefore, the lensing efficiency is about 0.0743 giant arcs per cluster at $z_1 = 0.2$ and 0.0563 giant arcs per cluster at $z_1 = 0.3$. We illustrate the lens redshift (z_1) dependence and the fluctuation of number counting in Fig. 9 for 20 randomly selected tiles. All the giant arcs ($L/W \geq 10$) produced by the 10 massive lens clusters from the galaxies in each tile are taken into account. The lensing probability appears to decrease from $z_1 = 0.2$ to $z_1 = 0.5$ in our case, although the fluctuation is relatively large mainly due to the difference of source properties between each tile and the intrinsic surface density fluctuations (e.g., between actual imaging region and white margin) within the tiles.

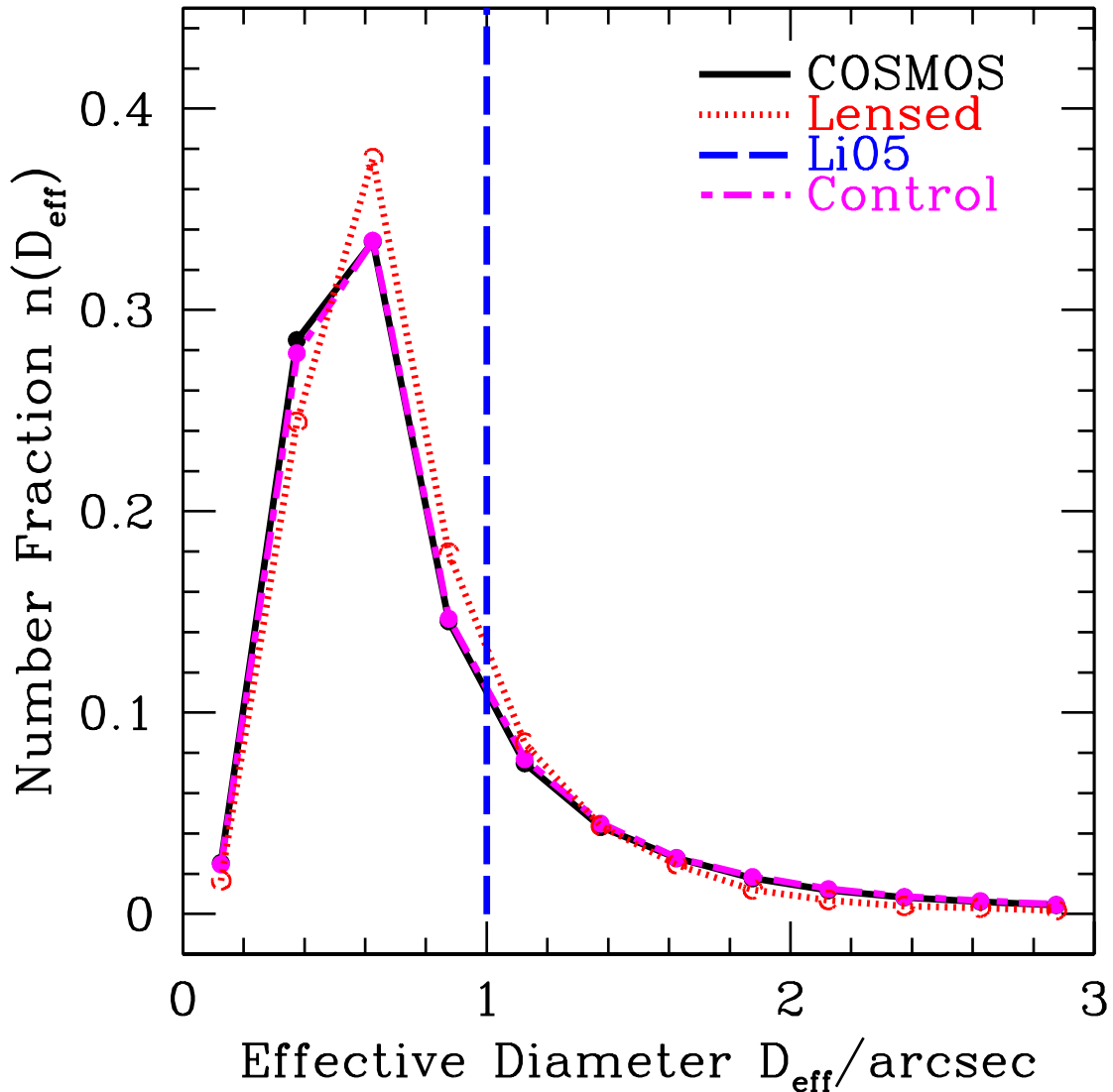


FIG. 6.— Comparison plot of size probability distributions between the subpopulation of original galaxies which have been strongly lensed to be arcs of $L/W \geq 10$ ($z_1 = 0.2$) and parent population of COSMOS galaxies. The number fractions per effective diameter bin of width $\Delta D_{\text{eff}} = 0.25$ arcsec are plotted. There is little difference between the two distributions, which indicates they share the almost same population. The size distribution of the fiducial control sample consisting of 100 randomly selected tiles (used in Table 1) is plotted in magenta. There is no big difference from the mean in most D_{eff} range, except the places around the peak. For comparison, the distribution used in Li et al. (2005) is also indicated.

4.1.1. Redshift influence

In recent works (Bartelmann et al. 1998; Li et al. 2005), the background sources are taken to be at the same redshift, e.g., $z = 1$, to estimate the theoretical overall efficiency of forming giant arcs in our universe. As shown in Fig. 4 the background sources in fact have a rather broad distribution, which we take into account by binning them into ~ 50 redshift slices. If we put all the sources into a single redshift plane at $z_s = 1$, we find that in this case the number of giant arcs ($L/W \geq 10$) increases by a factor of ~ 1.05 compared with Case 1 in Table 1, since the equivalent source redshift plane, in which we put all the source galaxies to generate similar number of giant arcs, for the 100 randomly selected COSMOS tiles (i.e., “fiducial control sample” tiles which are considered as the “seeds” to generate mock samples for cases in Table 1) is about 0.9 which is slightly lower than $z_s = 1.0$. Notice that the shape, size distributions and surface density follow the original distributions of COSMOS. Therefore, z_s plane is coincidentally a good approximation to the broad redshift distribution. However, according to Wambsganss et al. (2004) and Li et al. (2005), the lensing probability becomes larger when the sources are put at a higher redshift, which is also seen in the redshift distribution of lensed sources in Fig. 4 where the lensed galaxies, stretched to become giant arcs of $L/W > 10$, are clearly biased toward high redshift relative to the underlying background population. For comparison, the analytical

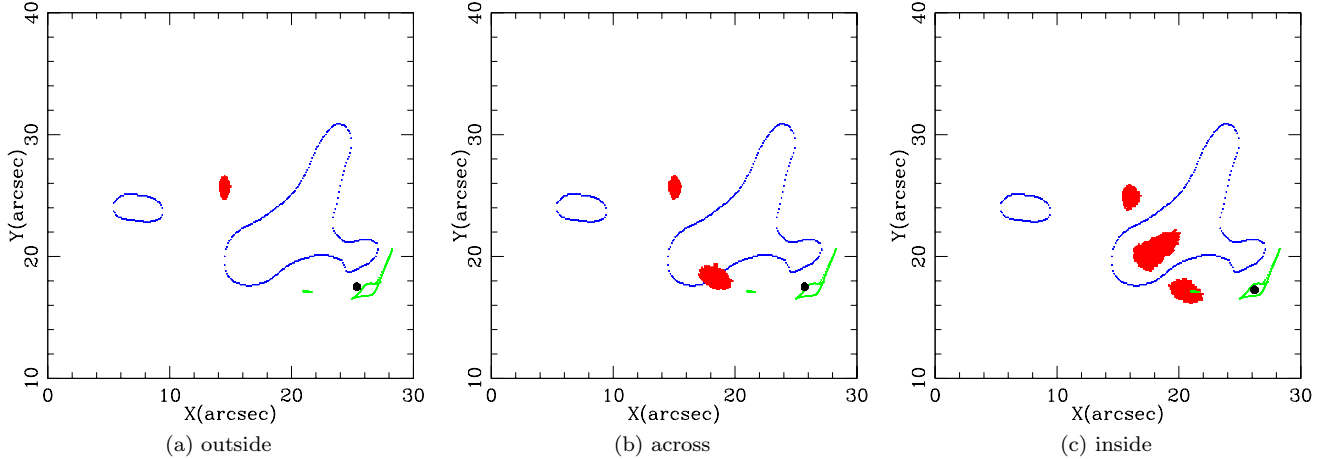


FIG. 7.—: Simulated images for a mocked circular galaxy located outside, on and inside the tangential caustic of a merging galaxy cluster, which is selected to illustrate for easy identification. The black dots indicate the sources, while the red ones are the lensed images. The green and blue dotted lines indicate the caustics and critical curves respectively. As can be seen, the lens produces single, double and triple strongly lensed images.

TABLE 1: Results of 7 different sets of simulations. “z”, “s” and “e” indicate the redshift, size and ellipticity of the background sources, while “1” and “0” represent following COSMOS and mocked. For example, “e0” implies the ellipticity (1-b/a) is randomly chosen in the range between 0 to 0.5. We run 10 lensing simulations in each projection of the 5 (middle) massive clusters at $z_1 = 0.2$ for each source tile. In each case, 100 tiles are selected to construct the control sample with required source properties. The redshift, ellipticity and size distributions of the selected COSMOS tiles are plotted in Fig. 4, 5 and 6, labeled as “Control”. There are 15000 ray-tracing realizations performed for each control sample. (Similar results are obtained for clusters at $z_1 = 0.3$).

Case	Name	z	s	e	N
1	z1s1e1	COSMOS	COSMOS	COSMOS	1204
2	z0s1e1	z=1.0	COSMOS	COSMOS	1264
3	z0s0e0	z=1.0	$D_{\text{eff}} = 1.0''$	RANDOM	321
4	z1s0e1	COSMOS	$D_{\text{eff}} = 1.0''$	COSMOS	852
5	z1s0e0	COSMOS	$D_{\text{eff}} = 1.0''$	RANDOM	369
6	z1s1e0	COSMOS	COSMOS	RANDOM	493
7	z0s1e1	z=1.5	COSMOS	COSMOS	1935

TABLE 2: Ray-tracing simulations are carried out for the massive clusters selected from two snapshots at redshift ~ 0.2 and ~ 0.3 . The cosmological model is a Λ CDM model with $\Omega_{\text{m},0} = 0.268$, $\Omega_{\Lambda,0} = 0.732$, $n = 1$, and $\sigma_8 = 0.85$. We implement 10 lensing simulations (marked as N_R) for each projection and each source tile. The whole simulation covers the full sample of 575 source tiles (marked as N_T).

Set	z_1	$M_{\text{vir}}(10^{14}h^{-1}M_{\odot})$	N_C	N_P	N_R	N_T
1	0.2	6.8-11	10	3	10	575
2	0.3	6.0-8.1	10	3	10	575

redshift distribution in Fedeli et al. (2008) is also shown in Fig. 4. If we adopt a source redshift distribution following a deeper galaxy survey like in Fedeli et al. (2008) (keeping other properties unchanged), the giant-arc number is increased by a factor ~ 2 , compared with the number of giant arcs when the COSMOS redshift distribution is used (Case 1 in Table 1).

However, the equivalent source redshift plane changes with source shape distributions. For example, considering the comparison cases, Cases 3 and 5 in Table 1, we find a higher equivalent source redshift (e.g., $z_s \sim 1.6$) for galaxies of simulated shapes as in Case 3 than those of the intrinsic shape distribution in Case 1, which share the same intrinsic redshift distribution. This can also be explained by Fig. 10. Galaxies of simulated ellipticities at higher redshift have a relatively higher weight than those of intrinsic ellipticities in producing giant arcs. It causes the equivalent source redshift for Case 5 to be larger than the mocked redshift in Case 3, e.g. $z_s = 1.0$, thus a higher lensing efficiency. Also, the redshift of equivalent source plane may shift to a higher redshift for a deeper survey. In this case, the lensing probability may increase substantially and a single source plane approximation (at $z_s = 1.0$) can become violated. For

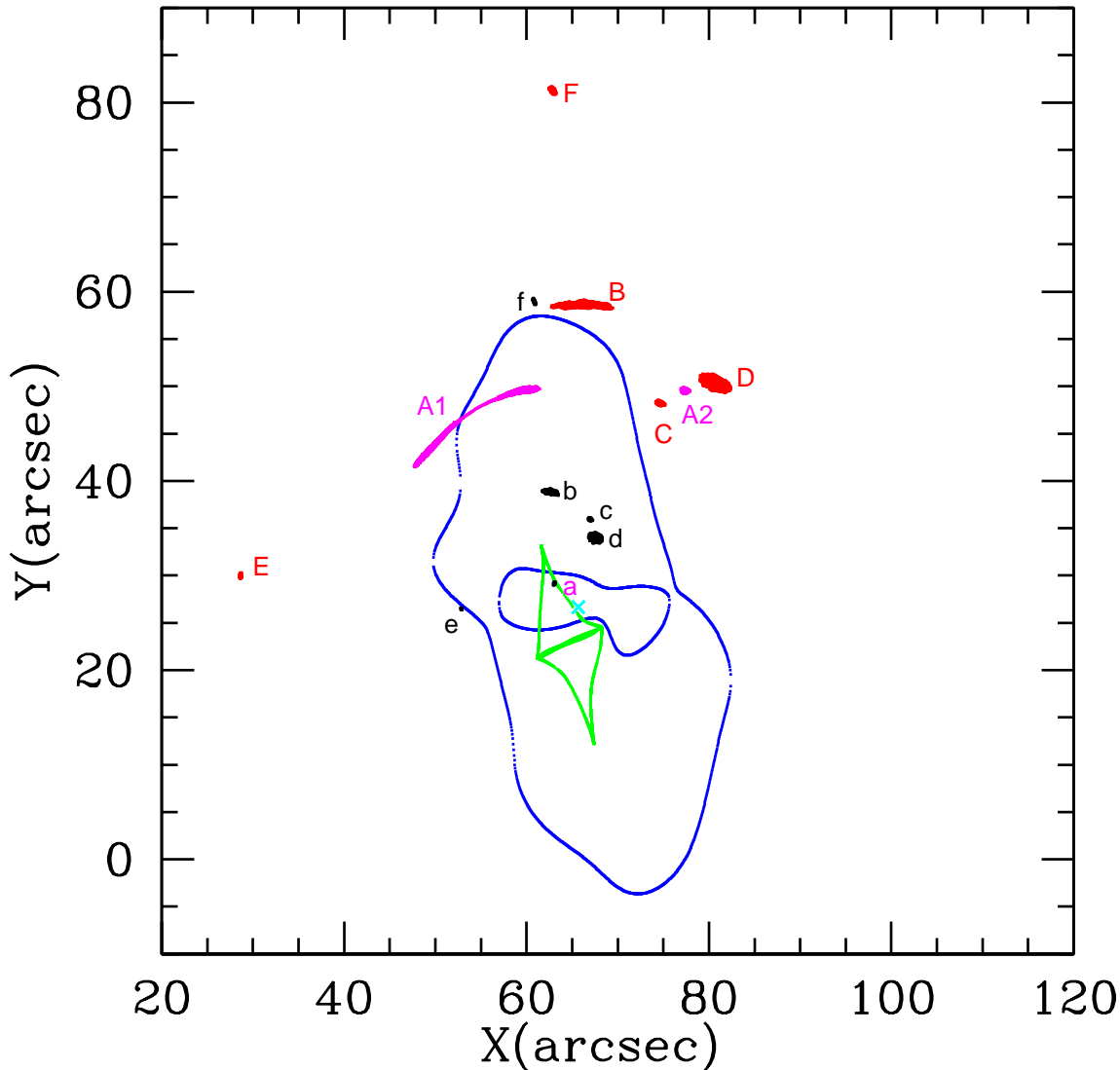


FIG. 8.— Simulated images by a massive lens cluster ($z_l = 0.3$) for galaxies in a COSMOS tile. The sources and their lensed images are shown in black and red respectively. The other unlensed galaxies in the tile are not plotted together for a clear view. The blue and green curves are critical lines and their corresponding caustics for sources at redshift $z_s = 3.0$, while the cyan cross indicates the center of lens. A strongly stretched arc “A1” is clearly seen corresponding to the source “a”; an additional image “A2” is highlighted (in magenta) for the same source.

example, we find an increase of a factor ~ 2 in giant-arc number for a mocked source sample following the analytical redshift distribution in Fedeli et al. (2008), which is shown in Fig. 4. It is necessary to take account of the full redshift distribution in predicting the strong lensing efficiency.

4.1.2. Source shape influence

Previous studies (Li et al. 2005; Puchwein et al. 2009) often assumed the sources follow a uniform distribution in the ellipticity ($\epsilon \equiv 1 - b/a$) between 0 and 0.5. However, as can be seen in Fig. 5, while it is true that the ellipticity $1 - b/a$ of most sources is less than 0.5, there is still a high fraction of sources, about 1/3, with ellipticity larger than 0.5. The sources with large ellipticities, such as edge-on spiral galaxies, could be stretched much more easily to form giant arcs of large L/W values when the tangential direction of the lens is approximately along the direction of the major axis of the background galaxy. Therefore, the small portion of high ellipticity sources may change the giant-arc statistics substantially.

For all the COSMOS sources in the fiducial control tiles, we change the shape of sources with random ellipticities (between 0 and 0.5) and orientations (between 0 and π) while keeping the source positions, sizes and redshifts unchanged. We perform a lensing simulation for this background galaxy sample. This case (Case 6) is labeled as “z1s1e0”. We find that the number of giant arcs is only $\sim 1/2$ of the value from the COSMOS sources. The shape influence is also

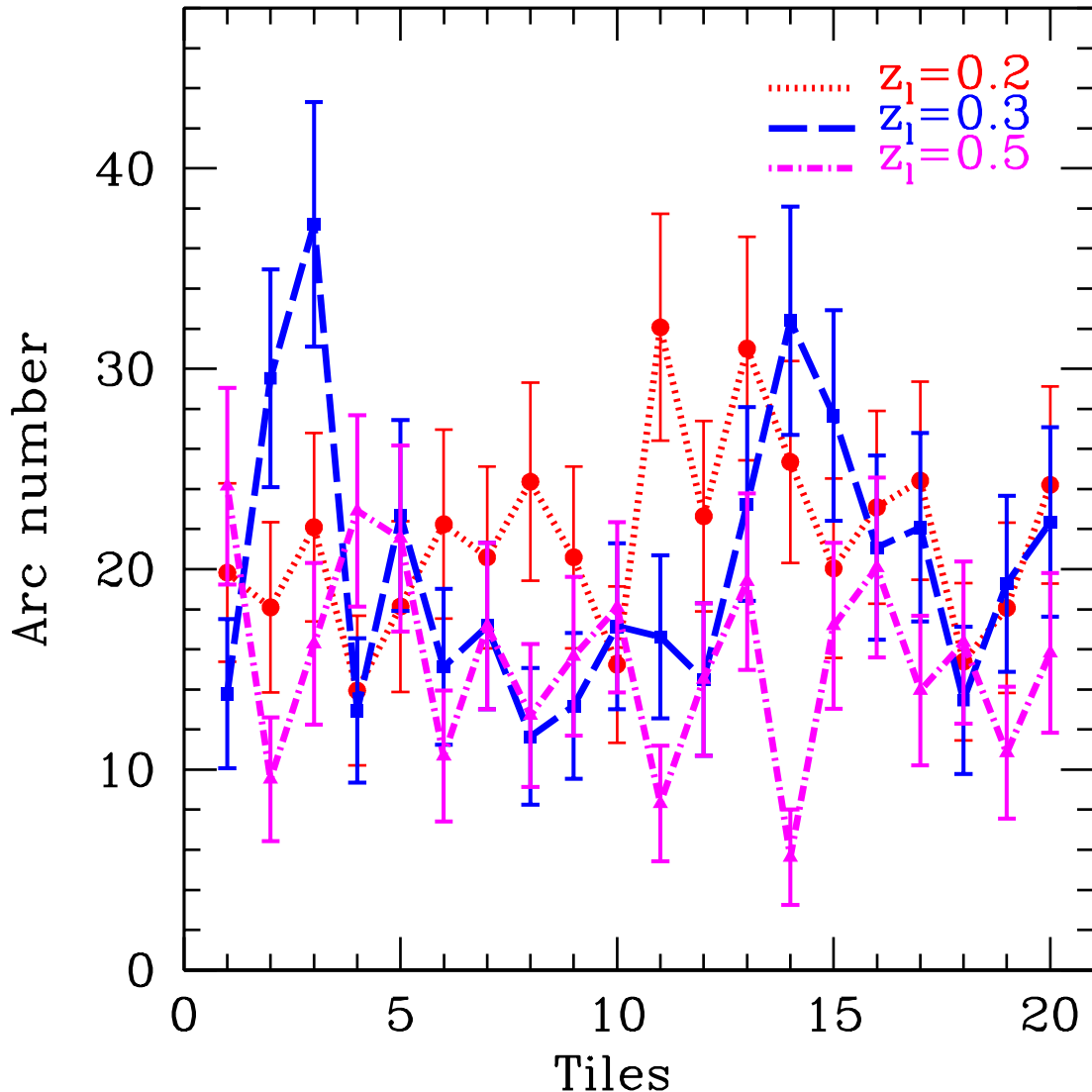


FIG. 9.— The giant-arc statistics for three test runs at different lens redshifts, e.g., $z_1 = 0.2$, 0.3 and 0.5 are illustrated. The 20 test source tiles are randomly selected. For each source tile, all the giant arcs produced in 300 realizations of 10 massive clusters are counted (see Table 2). As can be seen, the fluctuation is large for a single source tile in the mock survey due to the limited realizations. The lensing efficiency decreases when the lens redshift ranges from 0.2 to 0.5, which is consistent with the result in §4.5.

directly reflected in the different ellipticity distributions of the original COSMOS galaxies and the lensed population. As clearly seen in Fig. 5, the lensed population of original galaxies with giant arcs of $L/W > 10$ shows a clear shift to the higher ellipticity tail.

It is important to explore whether the effect of source shape changes with the source redshift. Although the overall cross-section becomes larger for a higher source redshift, the change of the effective lensing area, in which elongated sources can be lensed to giant arcs while the simulated ones of $0 \leq \epsilon \leq 0.5$ cannot be, is not clear. We construct 4 comparison pairs of control source samples generated from the fiducial control tiles, i.e. “z0s0e1” and “z0s0e0”, at redshift of $z_s = 0.8, 1.0, 1.5, 3.5$. As clearly seen in Fig. 10, while the number of giant arcs increases with the source redshift, the shape impact on lensing efficiency decreases from ~ 4 to ~ 2 , when source redshift ranges from $z_s = 0.8$ to 3.5. The boost effect of source shape is expected to be larger at z_s lower than 1.5 since the lensing cross-section is smaller at lower redshift and thus the enhancement due to the elliptical sources is relatively more important.

4.1.3. Source size influence

Instead of assuming a same effective diameter for all sources (Li et al. 2005; Puchwein et al. 2009), we have adopted the COSMOS galaxy sizes in our fiducial case (Case 1). To see the size effect of background galaxies, we first check the size distribution for the lensed galaxies which are stretched to be giant arcs of $L/W > 10$. The comparison results

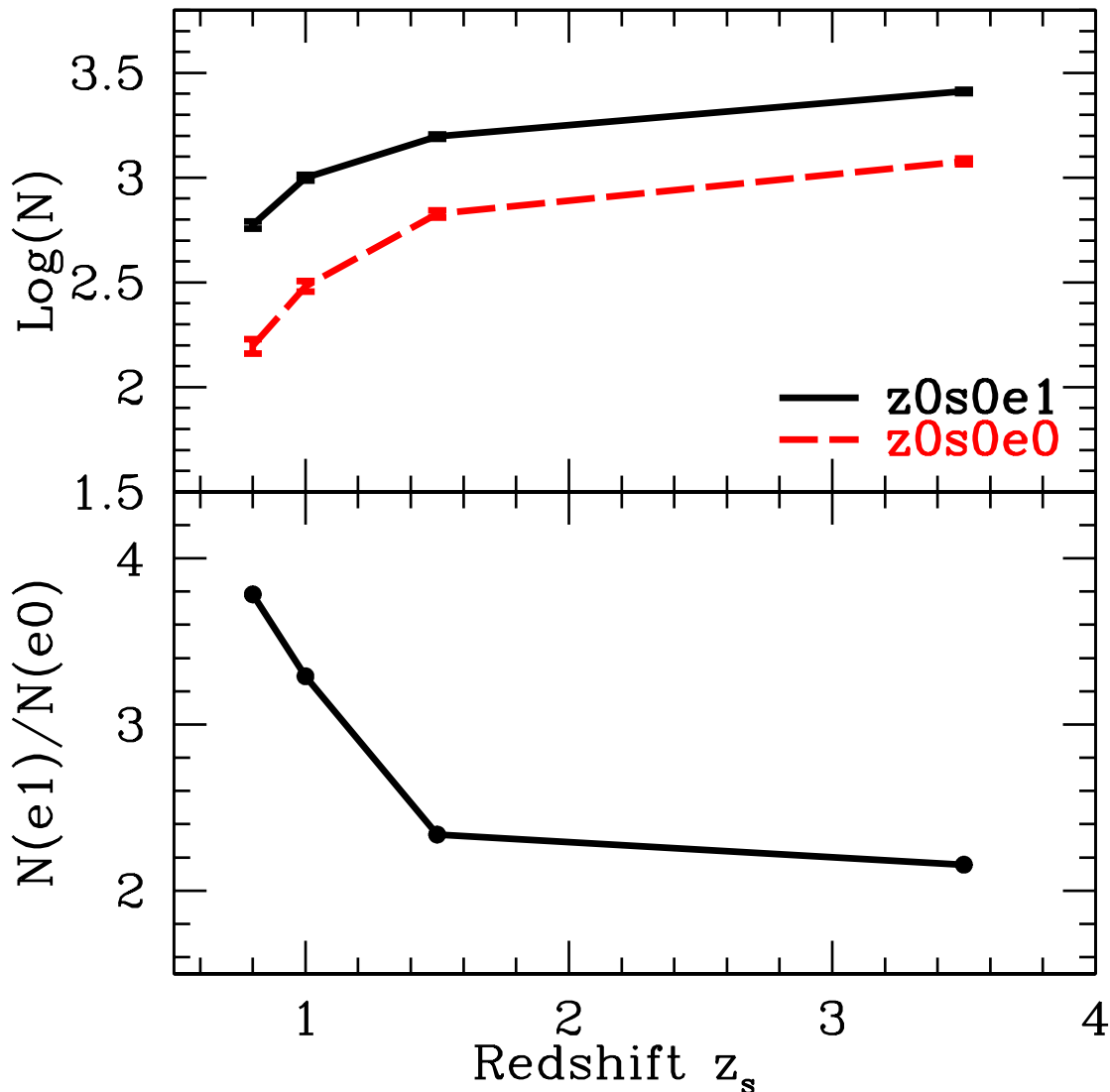


FIG. 10.—: The shape impact on cross-section dependence of z_s is illustrated. It is clearly seen that the lensing incidence is boosted after the real galaxy shape is adopted (top panel). The Poisson fluctuations are indicated as error bars in the panel. As a comparison, we put the sources of random ellipticity (shown in red) or real ellipticity (shown in black) in source planes at redshift $z = 0.8$, $z = 1.0$, $z = 1.5$ and $z = 3.5$, keeping source size of $D_{\text{eff}} = 1''$. While confirming the shape impact on lensing cross-section is about a factor of 2 for $z_s > 1.5$, with a larger factor at $z \lesssim 1$ (bottom panel).

are illustrated in Fig. 6, it shows that there is little difference between these two distributions, and thus the source size is expected to have small effect on producing giant arcs.

This is directly confirmed by two comparison samples, where we fix the effective diameters assigned to be $D_{\text{eff}} = 1.0''$ and $D_{\text{eff}} = 0.5''$. We find a similar number of giant arcs (188 and 166 out of 3000 realizations), which is consistent with Fig. 6. Source size thus has a moderate effect on producing giant arcs when massive clusters are taken as lenses (also see Fig. 3 and Fig. 11). The reason is that the typical source size is much smaller than the strong lensing caustic size, and thus a moderate change in the source size has a small impact on the number of giant arcs.

4.2. Combination of Morphology and Redshift Distribution

To see the overall impact of the simple assumptions for the shape, size, and redshift of background galaxies, we combine these effects to do lensing simulations (for random position effect, see §4.3). The redshift of all these sources is assigned to be 1.0. The shape with a random orientation (between 0 and π) are simulated as above, while the effective diameter is assigned to be $1''$. We find that the lensing efficiency for the Case 3 (“z0s0e0”) is a factor of 3.75 lower than that for Case 1 (“z1s1e1”). It is roughly consistent with the results from the combination of the individual effects, i.e. redshift effect (a factor of 1.15 which is got from comparing Case 3 and 5), shape effect (a factor of 2.31

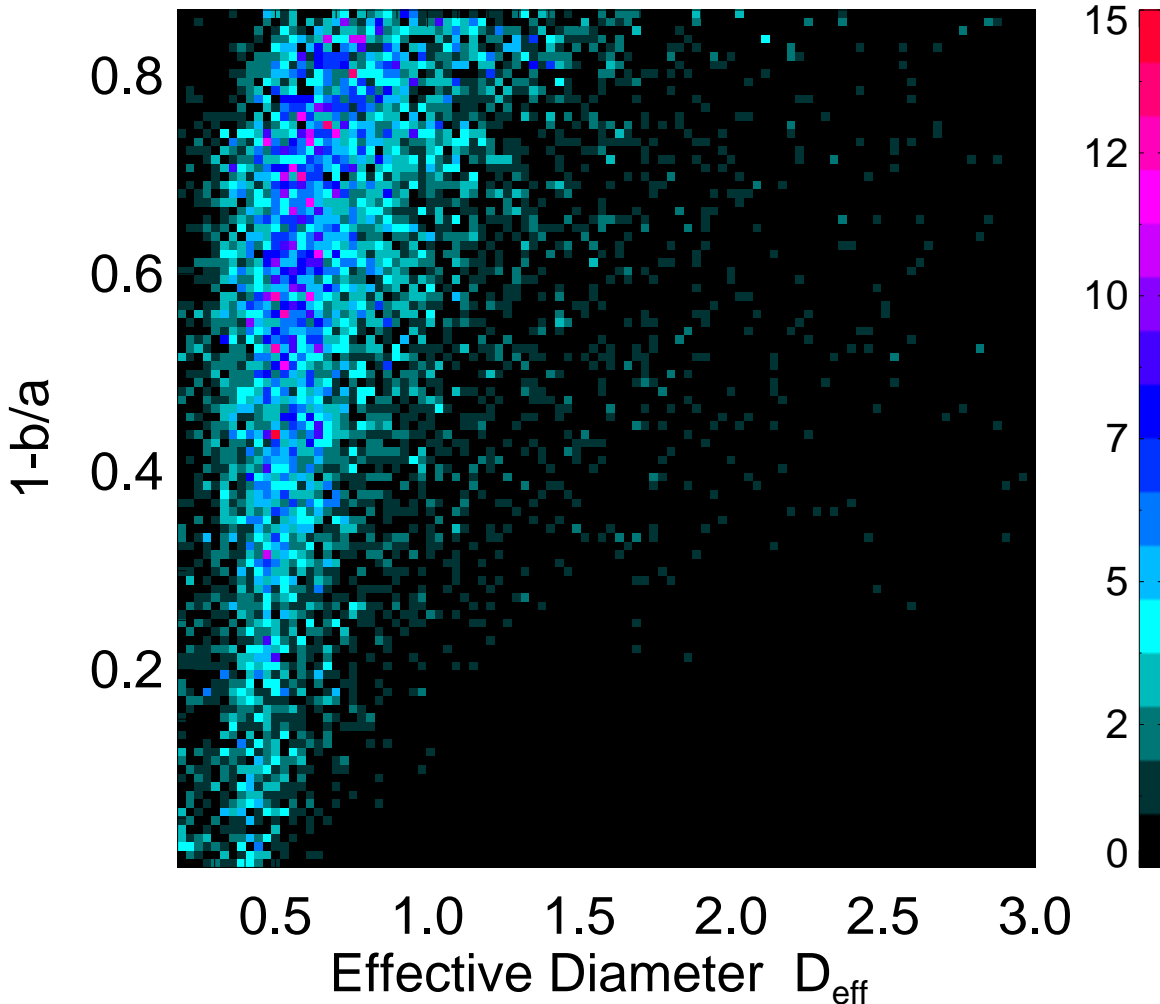


FIG. 11.—: The color-weighted distribution plot of the ellipticity against size for sources lensed to be images with $L/W \geq 10$. The lensed sample is obtained from tracing back all the giant arcs produced by 10 massive clusters at redshift $z \sim 0.2$. The pattern of the distribution is similar to that shown in Fig. 3, although the elongated sources have a higher weight, which is consistent with that implied in Fig. 5.

from Case 4 and 5) and size effect (a factor of 1.34 from Case 5 and 6), which is $1.15 \times 2.31 \times 1.34 = 3.56$. It thus indicates that the galaxy shape, redshift and size are affecting strong lensing efficiency independently as well as these three properties are independent of each other intrinsically as shown in Fig. 1, 2 and 3.

4.3. Effect of Source Clustering

Theoretical calculations often assume that the background sources are randomly distributed in space. However, background galaxies are clearly clustered. It is therefore interesting to check the effect of source clustering on the incidence of giant arcs.

The influence of the clustering effect is investigated by carrying out a ray-tracing simulation on a control sample of galaxies where the positions of original COSMOS galaxies in a fiducial tile are randomly shuffled while keeping the source surface density, size and ellipticity unchanged. We find that the efficiency of producing giant arcs (166 giant arcs out of 3000 realizations for 10 clusters at $z_1 = 0.3$) is similar to what obtained in the COSMOS case (163 giant arcs) which implies the clustering effect of background sources is negligible on strong lensing. The likely reason is that the intrinsic source density is too low (43 per square arcmin) and close pairs of sources are too few to form connected giant arcs or to be strongly lensed simultaneously. Our results suggest that sources can be assumed to be random in the prediction of giant arcs, at least to the depth of COSMOS (in deeper images with a larger source density, clustering may become more important).

4.4. Effects of Seeing in Ground-based Observations

For our fiducial simulation (Case 1), the observational data are taken by HST (as in the Hubble Deep Field used in Horesh et al. 2005). However, many giant arcs were discovered from the ground-based telescopes where the effect of seeing may be important. A proper evaluation would require a detailed simulation of seeing effects. Here we discuss briefly the approximate seeing effect on the predicted number of giant arcs.

In COSMOS, there is a significant portion ($\sim 80\%$) of small galaxies with the effective diameter $D_{\text{eff}} \leq 1''$ (see Fig. 6). The width of lensed giant arcs produced from these small sources probably remains less than $1''$. In such cases, seeing (such as $\sim 1''$) will have a much larger effect on the width of giant arcs than on the length (Meneghetti et al. 2007), and in general the L/W ratio will be substantially reduced. Assume the seeing is $\sim 0.5''$, the width of arcs intrinsically smaller than $0.5''$ will be blurred to $\sim 0.5''$ which we adopt as the “observed” width. We find that in this case the fraction of giant arcs of $L/W \geq 10$ will be reduced to 80% of the COSMOS value. If seeing is as bad as $1''$, the lensing probability could be reduced to about 40% of the original value. Although this is only an approximate estimation, it is clear that the impact of seeing should be carefully evaluated in a detailed comparison between theoretical predictions and ground-based giant-arc surveys.

4.5. Comparison with Observations and Horesh et al. (2005)

The giant arcs in this work are selected by quantifying the ratio of length to width ($L/W \geq 10$). The definition of L/W in this paper is the same as that in Li et al. (2005). As a mock strong lensing survey, we have done 172500 realizations of ray-tracing simulations for all the 10 lens clusters at $z_1 = 0.2$ or $z_1 = 0.3$ with 575 galaxy tiles, and find that the lensing efficiency is about ~ 0.0743 arcs for clusters at $z_1 = 0.2$ and ~ 0.0563 arcs for clusters at $z_1 = 0.3$ per realization.

On the face value, they are much lower than the expected mean probability of ~ 1 giant arc per realization (Horesh et al. 2005). However, they adopted galaxy images in the Hubble Deep Field whose source density is about 12 times higher ($1378/5.3=260 \text{ arcmin}^{-2}$ in HDF, vs. 23 arcmin^{-2} in our case). The lensing efficiency with the surface density normalized is 0.840 arcs and 0.636 per realization, respectively. Horesh et al. (2005) used a different definition of L/W ratio which is smaller than ours by a factor of $4/\pi$ (e.g., their $L/W \geq 10$ is equivalent to our $L/W \geq 2.5\pi \approx 7.5$), and thus our lensing efficiency (of $L/W \geq 10$) will be boosted by a factor of $(4/\pi)^2$ if we adopt their length-to-width ratio definition. Taken these two factors into account, our clusters produce $0.840 \times (4/\pi)^2 = 1.36$ and $0.636 \times (4/\pi)^2 = 1.03$ giant arcs per realization for $z_1 = 0.2$ and 0.3 , respectively. In this exercise, we have assumed that the giant arc formation cross-section scales as the magnification probability distribution ($p(> |\mu|) \propto \mu^{-2}, |\mu| \gg 1$). Therefore, the capability of our simulated lens clusters is in fact consistent with the observation, which is about 1.2 arcs per cluster found by Horesh et al. (2005) using the sample in Smith et al. (2005).

The slight excess in the number counting could be induced by small number statistics and the relatively narrow mass range of the simulated lenses by contrast to the observational clusters. It also could be due to the different lens redshift distributions of the simulated ($z_1 \sim 0.2$) and observational samples ($0.171 < z_c < 0.255$).

5. SUMMARY AND DISCUSSION

In this paper, aiming to study the impacts of background sources on strong lensing statistics, we use the I -band galaxy image data of HST/ACS in the COSMOS to quantify the distributions of background source size, shape and redshift. Each galaxy image is extracted by SExtractor limiting a surface brightness down to $\sim 25 \text{ mag/arcsec}^2$. The redshift of each galaxy image is obtained by matching its celestial position with the COSMOS photometric catalog. The selected sources are then lensed by 10 massive clusters of the mass range $6.8 \times 10^{14} h^{-1} M_{\odot} \leq M_{\text{vir}} \leq 1.1 \times 10^{15} h^{-1} M_{\odot}$ at $z_1 \sim 0.2$ and $6.0 \times 10^{14} h^{-1} M_{\odot} \leq M_{\text{vir}} \leq 8.1 \times 10^{14} h^{-1} M_{\odot}$ at $z_1 \sim 0.3$ as the lensing clusters chosen from a cosmological simulation in the Λ CDM cosmology ($\Omega_{\text{m},0} = 0.268, \Omega_{\Lambda,0} = 0.732$). 575 source tiles within the COSMOS field of around 2 deg^2 are fully used for the statistic study. 172500 ray-tracing lensing simulations are carried out for 10 lens clusters to reduce the statistical fluctuation at the expected lens redshifts (i.e. $z_1 = 0.2$ and 0.3). The incidence of giant-arc production in our simulation is roughly consistent with that observed in Smith et al. (2005), after the density difference is taken into account. The impacts of source size, shape and redshift on strong lensing statistics are investigated in detail.

We find that the source size (less than a factor of 1.5) and clustering only have small effects on the production of giant arcs. In contrast, the dependencies on the source redshift and ellipticity are much more significant. The first was highlighted by Wambsganss et al. (2004), while the second is the main new finding of the current work. We find that adopting the empirical ellipticity distribution of COSMOS increases the lensing probability by a factor of 2 (see Fig. 10 and also the number ratio between Case 1 and 6). The boosting effect of the ellipticity of the background galaxies has not been emphasized in the previous works. It should be included in theoretical modeling of giant arcs in future. This may also be of particular relevance for setting constraints on the power-spectrum normalization parameter σ_8 .

There are a number of limitations in the present work. When scaling our results with the source number density, we implicitly assume that other source properties (like ellipticity and redshift) are the same in COSMOS as in a deeper observation (like HDF). However, ellipticity distribution of galaxies in a deeper survey may turn out to be more elliptical (Vincent et al. 2005; see also the discussion on the surface brightness limit), which would increase the boosting factor of source ellipticity on strong lensing efficiency. We would also have a larger fraction of galaxies at the high redshift tail end in a galaxy survey like HDF, which increases the mean strong lensing cross section. Therefore,

both effects will produce more giant arcs. For direct comparison with observation, the observational effects, such as specific instrumental point-spread-function and observational seeing, are not fully included in our lensing simulations. As mentioned in §4.4, if the seeing was $1''$, then there may be only around 40% of giant arcs observed by a typical ground-based telescope compared with that by space-based one, such as HST.

The same shape measurement method is used for quantifying the ellipticity of the original galaxies and lensed images. It could bring in some inaccuracy for measuring the ellipticity of very round images, since it is mainly designed for quantifying arcs. Nevertheless, this effect is rather small and negligible to our results, since we mainly focus on the elliptical galaxies. Besides, the intrinsic pixelization will affect the ellipticity quantification of small sources, especially for sources of $D_{\text{eff}} < 0.3''$ (see Fig. 3). The influence of pixelization would probably shift down the measured ellipticity because of its relative larger effect on width measurement. Since the number of such tiny sources is small ($\sim 5\%$) and the pixelization does not significantly change the ellipticity value on average (much smaller than the effect of seeing), this influence would not be important to our analysis.

According to Torri et al. (2004), cluster substructures are important for strong lensing efficiency in a major merger case, especially at the early state. As we adopt a softening length of $30 h^{-1}\text{kpc}$, the softening mainly takes effect in the center of major merging clumps, while it would also smooth away the small substructures of a similar scale in a minor merger case or those remaining in a main halo. The change of the lensing cross section due to this kind of smoothing would not be significant in both cases. Besides, according to a comparison plot of optical depth in Fig. 4 of Li et al. (2005), the result agrees within 25% of Wambsganss et al. (2004), in which they adopt a much smaller softening length of $3.2h^{-1}\text{kpc}$ than $30 h^{-1}\text{kpc}$ in our case, for a source redshift of $z_s = 1.0$. Therefore, although the relatively large value of softening length could reduce the lensing efficiency, it would not affect our results significantly. Moreover, lensing clusters are selected from a dark matter only simulation, therefore, we cannot investigate the strong lensing dependence on source properties for clusters with realistic baryon distributions.

We have only used one surface brightness limit (e.g., a detection threshold of 1.5σ) to extract the background galaxy images. Since the redshift of galaxy is mainly constrained by the matching with photometric catalog, it will not change the distribution by using a higher detection threshold in our case. A variation of detection threshold would change the galaxy size, but the dependence of lensing efficiency on source size is weak (see §4.1.3), thus the main results should remain unchanged. The source shape distribution also depends on the surface brightness threshold. Indeed, at a lower surface brightness limit, the shape of the galaxies tends to more elliptical (Vincent et al. 2005). Thus at fainter surface brightness, the shape influence is expected to play a more important role on giant-arc production for the same lens cluster population. It is meaningful to do ray-tracing experiments by using several surface brightness limits to quantify the shape impact on strong lensing in different survey depths.

The different mass range of the simulated clusters and X-ray selected ones could bring in quantitative uncertainties in the giant-arc statistics, since the strong lensing cross section strongly depend on mass, e.g., the mean cross section changes by nearly 4 orders of magnitude over mass ranging from $10^{14} h^{-1}M_{\odot}$ to $\sim 10^{15} h^{-1}M_{\odot}$ in Fig. 7 of Hennawi et al. (2007a). However, the mean cross section ratio is less than 1.5 between the observed and our simulated clusters, according to the plot. Moreover, they use a larger mass density parameter $\Omega_{\text{m},0} = 0.3$ and a higher matter power-spectrum normalization $\sigma_8 = 0.95$ in their simulation. Besides, the simulated clusters are put at a much higher redshift $z_1 = 0.41$. All these effects help to make the mass dependence of lensing probability stronger. Therefore, the difference of mean cross section in two comparing samples would be much less than a factor of 1.5 and becomes negligible in this work. Nevertheless, it is still necessary and interesting to select more comparable (between the simulated and X-ray selected) lens cluster samples in mass and redshift range for a fair comparison of giant-arc producing efficiency in the future.

ACKNOWLEDGMENT

We would like to thank the anonymous referee for his/her useful suggestions. We also thank W. P. Lin for managing the large amount of the data and helpful discussions. This work is supported by NSFC (10533030, 10821302, 10878001), by the Knowledge Innovation Program of CAS (No. KJCX2-YW-T05), and by 973 Program (No. 2007CB815402). GL is supported by the Humboldt Foundation. SM acknowledges the Chinese Academy of Sciences and the Chinese National Science Foundation for travel support. This work was also partly supported by the visitor's grant at Jodrell Bank, a joint research grant from the NSFC and the Royal Society, the Department of Energy contract DE-AC02-76SF00515 and by the European Community's Sixth Framework Marie Curie Research Training Network Programme, Contract No. MRTN-CT-2004-505183 "ANGLES".

REFERENCES

- Bartelmann, M., Huss, A., Colberg, J., Jenkins, A., Pearce, F. 1998, *A&A*, 330, 1
 Bertin, E., Arnouts, S. 1996, *A&AS*, 117, 393
 Broadhurst, T., Barkana, R. 2008, *MNRAS*, 390, 1647
 Bryan, G. L., Norman, M. L. 1998, *ApJ*, 495, 80
 Comerford J. M., Meneghetti M., Bartelmann M., Schirmer M. 2006, *ApJ*, 642, 39
 Dalal, N., Holder, G., Hennawi, J. F. 2004, *ApJ*, 609, 50
 Dolag, K., Vazza, F., Brunetti, G., & Tormen, G. 2005, *MNRAS*, 364, 753
 Fedeli, C., Bartelmann, M., Meneghetti, M., Moscardini, L. 2008, *A&A*, 486, 35
 Ferguson, H. et al. 2004, *ApJ*, 600, L107
 Fernández-Soto, A., Lanzetta, K. M., & Yahil, A. 1999, *ApJ*, 513, 34
 Gladders, M. D., Hoekstra, H., Yee H. K. C., Hall, P. B., Barrientos, L. F. 2003, *ApJ*, 593, 48
 Hennawi, J. F., et al. 2006, *AJ*135, 664
 Hennawi, J. F., Dalal, N., Bode, P., Ostriker, J. P. 2007a, *ApJ*, 654, 714
 Hennawi, J. F., Dalal, N., Bode, P. 2007b, *ApJ*, 654, 93

- Hilbert, Stefan, White, Simon D. M., Hartlap, Jan, Schneider, Peter 2007, MNRAS, 382, 121H
- Horesh, A., Ofek, E. O., Maoz, D., Bartelmann, M., Meneghetti, M., Rix, H. W. 2005, ApJ, 633, 768
- Jing, Y. P., Suto, Y. 2002, ApJ, 574, 538
- Jing, Y. P., Suto, Y., Mo, H. J. 2007, ApJ, 657, 664J
- Kitayama, T., Suto, Y., 1996, MNRAS, 280, 638
- Koekemoer, A. M., Aussel, H., Calzetti, D., Capak, P., Giavalisco, M., Kneib, J.-P., Leauthaud, A., Le Fèvre, O., McCracken, H. J., Massey, R., Mobasher, B., Rhodes, J., Scoville, N., Shopbell, P. L. 2007, ApJS, 172, 197k
- Li, G. L., Mao, S., Jing Y. P., Bartelmann, M., Kang, X., Meneghetti, M. 2005 ApJ, 635, 795
- Li, G. L., Mao, S., Jing, Y. P., Kang, X., Bartelmann, M. 2006a ApJ, 652, 43
- Li, G. L., Mao, S., Jing, Y. P., Mo, H. J., Gao, L., Lin W. P. 2006b MNRAS, 372, L73
- Lopes, A. M., Miller, L. 2004, MNRAS, 348, 519
- Luppino, G. A., Gioia, I. M., Hammer, F., Le Fèvre, O., Annis, J. A. 1999, AAS, 136, 117
- Mao, S., Witt, H. J., Koopmans, L. V. E. 2001, MNRAS, 323, 301
- Mobasher, B., Capak, P., Scoville, N. Z., Dahlen, T., Salvato, M., Aussel, H., Thompson, D. J., Feldmann, R., Tasca, L., Lefevre, O., Lilly, S., Carollo, C. M., Kartaltepe, J. S., McCracken, H., Mould, J., Renzini, A., Sanders, D. B., Shopbell, P. L., Taniguchi, Y., Ajiki, M., Shioya, Y., Contini, T., Giavalisco, M., Ilbert, O., Iovino, A., Le Brun, V., Mainieri, V., Mignoli, M., Scodreggio, M. 2007, ApJS, 172, 117
- Melchior, P., Meneghetti, M., Bartelmann, M. 2007, A&A, 463, 1215
- Meneghetti, M., Bartelmann, M., Moscardini, L. 2003a, MNRAS, 340, 105
- Meneghetti, M., Bartelmann, M., Moscardini, L. 2003b, MNRAS, 346, 67
- Meneghetti, M., Melchio, P., Grazian, A., Lucia, G., Dolag, K., Bartelmann, M., Heymans, C., Moscardini, L., Radovich, M. 2007, arXiv0711.3418M
- Monaghan, J. 1992, ARA&A, 30, 543
- Navarro, J., Frenk, C., & White, S. 1997, ApJ, 490, 493
- Neto, A. F. et al. 2007, MNRAS, 381, 1450
- Oguri, M., Lee, J., Suto, Y. 2003, ApJ, 599, 7
- Oguri, M., Blandford, R. 2008, MNRAS, 392, 930
- Puchwein, E., Bartelmann, M., Dolag, K., & Meneghetti, M. 2005, A&A, 442, 405
- Puchwein, E., Hilbert, S. 2009, arXiv:0904.0253
- Reiprich, T., Böhringer, H. 2002, ApJ, 567, 716
- Sand, D. J., True, T., Ellis, R. S., Smith, G. P. 2005, ApJ, 627, 32
- Seljak, U., Zaldarriaga, M. 1996, ApJ, 469, 437
- Smail, I., Hogg, D. W., Yan, L., & Cohen, J. G. 1995, ApJ, 449, L105
- Smith, G. P., Kneib, J.-P., Smail, I., Mazzotta, P., Ebeling, H., & Czoske, O. 2005, MNRAS, 359, 417
- Stanek, R., Evrard, A. E., Böhringer, H., Schuecker, P., Nord, B. 2006, ApJ, 648, 956
- Torri, E., Meneghetti, M., Bartelmann, M., Moscardini, L., Rasia, E., Tormen, G. 2004, MNRAS, 349, 476
- Vincent, R. A., Ryden, B. S., 2005, AJ, 623, 137
- Wambsganss, J., Bode, P., Ostriker, J. P. 2004, ApJ, 606, L93
- Williams, R. E., et al. 1996, AJ, 112, 1335
- Zaritsky, D. Gonzalez, A. H. 2003, ApJ, 584, 691